



Short communication

Microspheres assembled by KMnO_4 nanorods and their catalytic oxygen reduction activity in direct methanol fuel cells

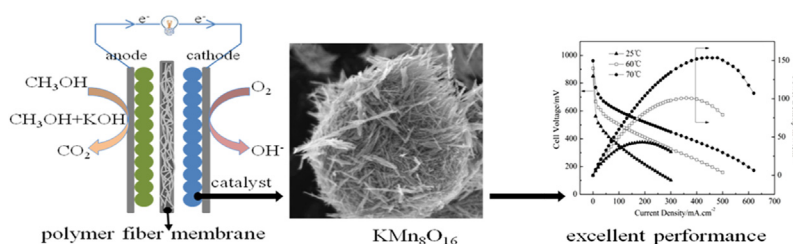
Yuan Fang, Xiaodong Yang, Li Wang, Yongning Liu^{*}

State Key Laboratory for Mechanical Behavior of Materials, Xi'an Jiaotong University, Xi'an 710049, PR China

HIGHLIGHTS

- KMnO_4 microspheres are assembled by nanorods with length of 300–1000 nm.
- The KMnO_4 shows excellent tolerance toward methanol poisoning and good stability.
- The electron transfer number was measured to be about 3.98 by RRDE.
- The cost of our novel alkaline DMFC is half of conventional DMFCs.
- The performance approaches the highest value of DMFCs with noble catalysts.

GRAPHICAL ABSTRACT



ARTICLE INFO

Article history:

Received 2 January 2014
 Received in revised form
 16 April 2014
 Accepted 17 April 2014
 Available online 4 May 2014

Keywords:

KMnO_4
 Oxygen reduction reaction
 Methanol tolerance
 Direct methanol fuel cell

ABSTRACT

Microspheres assembled using cryptomelane-type KMnO_4 nanorods are synthesized via a facile template-free, single-step hydrothermal technique. The synthesized KMnO_4 generates nanorods 10–20 nm in diameter and approximately 300–1000 nm long. The rods self-assemble to form microspheres of 2–6 μm in diameters. The electron transfer number for KMnO_4 during the ORR is approximately 3.98 at 0.5 V vs. Hg/HgO , and the H_2O_2 percentage is 0.66%. Moreover, a direct methanol fuel cell (DMFC) is built using KMnO_4 as cathodic catalyst, PtRu/C alloy as the anodic catalyst and a polymer fiber membrane (PFM) instead of a conventional polymer electrolyte membrane (PEM). The peak power densities (43.3 mW cm^{-2} and 153.9 mW cm^{-2}) have been achieved at 25 °C and 70 °C, respectively. KMnO_4 shows good electrocatalytic activity and stability during oxygen reduction in alkaline solutions and demonstrates tolerance toward methanol poisoning.

© 2014 Elsevier B.V. All rights reserved.

1. Introduction

Fuel cells convert chemical energy directly into electrical energy, making them promising energy-generating devices in industry, housing and traffic. Among them, direct methanol fuel cells (DMFCs) are gaining considerable interest due to their high energy density (6100 Wh kg^{-1} at 25 °C), low-to-zero emission and

relatively low operating temperature [1–4]. Moreover, methanol is easy to deliver and store, quick to refuel and low cost [5]. However, several challenges, including the sluggish oxygen reduction reaction (ORR) and methanol oxidation reaction (MOR) kinetics, as well as the high cost of the Pt catalyst and polymer electrolyte membrane (PEM), impede the commercialization of DMFCs [3,6,7].

Recently, a type of polymer fiber membrane (PFM) has demonstrated improved performance at a reduced cost in liquid fuel cells; this material is an excellent alternative to PEM in DMFCs and DBFCs [8,9]. PFM are liquid-permeable membranes. The fibers in these membranes are neutral, in which the pores and gaps allow

^{*} Corresponding author. Tel.: +86 29 8266 4602; fax: +86 29 8266 3453.
 E-mail address: ynliu@mail.xjtu.edu.cn (Y. Liu).

liquid fuel and ions to transport or move through the PFM freely. If methanol passes through the membrane from the anode to the cathode, it should be converted into carbon dioxide by cathodic catalysts, such as Pt or Pt-based alloys, creating a mixed potential at the cathode [2,10–13]. Therefore, the cathodic catalysts must have excellent tolerance toward methanol poisoning in addition to good stability.

To overcome this issue and achieve an acceptable power output, we are developing a methanol-tolerant and non-noble oxygen reduction catalyst. Many studies have focused on Pt-free catalysts, such as Pd–Co [14], Pd–Fe [15], Ir–Se chalcogenide [16], RuSe/CNT [17], ordered mesoporous carbon nitride [18], Fe–CA–N [19] and Co–CA–N [19]; these catalysts have ORR catalytical activity and can tolerate methanol.

In recent years, manganese-based oxides (MnO_2 , $\text{Li}_x\text{Mn}_2\text{O}_4$, etc.) have received increasing attention due to their abundance, non-toxicity and environmental friendliness during many technological applications [20–23]. The ORR activities of MnO_2 in alkaline media have been researched, and its catalytic activity strongly depends on the crystal structures [24]. Among the various forms of manganese-based oxides, we are interested in cryptomelane-type $\text{KMn}_8\text{O}_{16}$; this mixed-valent compound primarily contains Mn^{4+} with a small fraction of Mn^{3+} [25]. Structurally, the cryptomelane-type $\text{KMn}_8\text{O}_{16}$ materials have an octahedral molecular sieve (OMS) structure built from double chains of edge-sharing MnO_6 octahedra, forming $(2 \times 2) + (1 \times 1)$ tunnel structures with K^+ situated in the large (2×2) tunnels [26].

Several reports have detailed preparative methods for cryptomelane-type OMS, such as microwave heating, reflux and hydrothermal treatment, possibly generating different morphologies, particle sizes and particle distributions [27–31]. Cryptomelane-type $\text{KMn}_8\text{O}_{16}$ shows promising utility as an electrode material for rechargeable lithium batteries [28,31], and a catalyst for oxidizing harmful organic substances, such as formaldehyde [29], styrene [32] and olefins [33].

In this work, we report the ORR activity and methanol tolerance of $\text{KMn}_8\text{O}_{16}$ in a new DMFC system. In this DMFC system, we used $\text{KMn}_8\text{O}_{16}$ to catalyze ORR, PtRu/C as an anodic catalyst and PFM as a replacement for PEM; this system delivered a promising performance and good stability compared to the literature data. The $\text{KMn}_8\text{O}_{16}$ nanorods were prepared using a facile, template-free and single-step hydrothermal process. The crystal structure, morphology and electrochemical properties of the nanorods were studied.

2. Experimental

2.1. Catalyst preparation and characterization

All reagents were analytical grade. Cryptomelane-type $\text{KMn}_8\text{O}_{16}$ were prepared using a template-free, single-step hydrothermal process. $\text{MnSO}_4 \cdot \text{H}_2\text{O}$ (1.7 g) and KMnO_4 (2 g) were each dissolved in 40 mL of distilled water containing 1 mL of concentrated HNO_3 to provide an aqueous reaction medium. The solution was stirred vigorously at room temperature for 30 min, immediately forming a dark brown precipitation. The resulting suspension was transferred into a Teflon-lined stainless steel autoclave, sealed and maintained at 80, 100 and 120 °C for 24 h without shaking or stirring. After the mixture was cooled to room temperature, the brown precipitate was washed with distilled water several times and dried overnight at 80 °C. The three representative samples were designated KMO-80, KMO-100 and KMO-120 and were synthesized at 80, 100 and 120 °C, respectively.

The PtRu/C (HiSpec 10000) was purchased from Johnson Matthey (UK). The PFM (thickness = 159.3 μm) was purchased from the

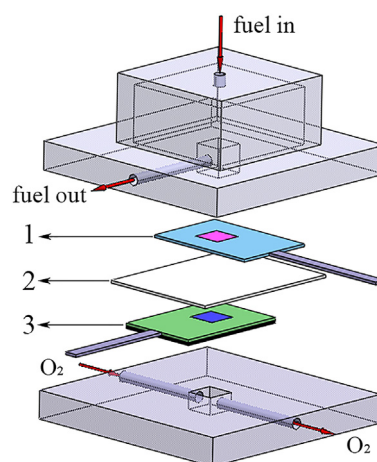


Fig. 1. The schematic of DMFC structure. 1 Anode electrode (azure blue) and anode active layer (red, 1 cm \times 1 cm); 2 PFM; 3 cathode electrode, consisting of an active layer (blue, 1 cm \times 1 cm), a gas diffusion layer (black) and a current accumulating matrix (green). (For interpretation of the references to color in this figure legend, the reader is referred to the web version of this article.)

Nippon Kodoshi Corporation. The structure and physical properties of the PFM are described in the supplementary information of our previous work [9]. The samples of MnO_2 and Pt/C (HiSpec 3000) used for comparison were purchased from J&K Chemical Ltd. and Johnson Matthey (UK), respectively.

The structure and composition of the prepared $\text{KMn}_8\text{O}_{16}$ powders were investigated with an X-ray diffractometer (XRD, Xpert-PRO, Holland) and energy-dispersive X-ray spectrometers (EDXS, OXFORD INCA300). The morphology of the samples was observed using field-emission scanning electron microscopy (FESEM, JSM-6700F, JEOL, Japan) and transmission electron microscopy (TEM, JEM-200CX, NEC, Japan). The Brunauer–Emmett–Teller (BET) surface areas and pore sizes of the as-prepared samples were measured using a nitrogen adsorption instrument (Micromeritics ASAP 2020).

2.2. Electrode preparation

The cathode for the DMFCs with PFM consisted of a gas diffusion layer, a current collector and an active layer. To prepare the gas diffusion layer, 60 wt.% acetylene black and 40 wt.% polytetrafluoroethylene (PTFE) (60 wt.% PTFE solution) with

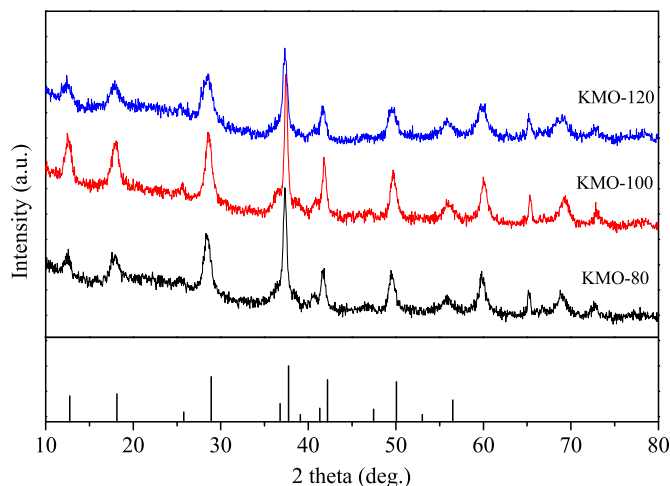


Fig. 2. XRD patterns for the KMO-80, KMO-100 and KMO-120 samples, respectively.

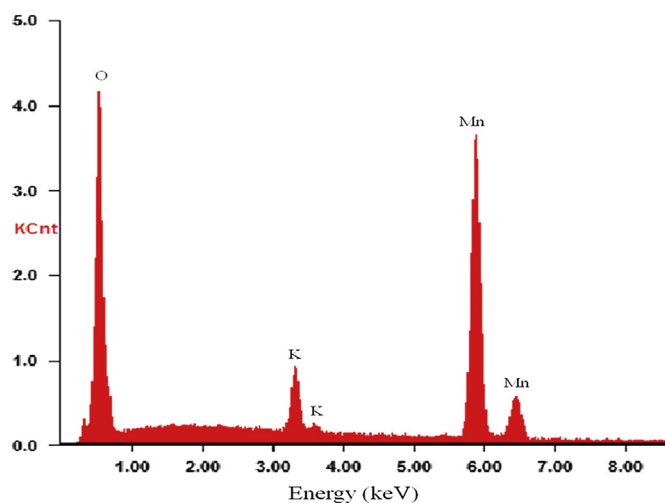


Fig. 3. EDXS result for the KMO-100 sample.

ethanol were mixed into a slurry. The slurry was then pressed into a 0.3 mm membrane and subsequently heated at 340 °C for 1 h. The active layer was prepared by mechanically mixing 30 wt.% catalyst, 45 wt.% carbon nanotubes (CNTs) and 25 wt.% PTFE (30 wt.% PTFE solution) with ethanol into ink. Next, the ink was smeared onto a current collector (nickel foam) and dried at 80 °C for 2 h under vacuum. The cathode was finished by pressing the gas diffusion layer and the prepared current collector under 2 MPa of pressure. The loading of the cathodic catalyst was 7.5 mg cm⁻².

The anode was prepared by mixing 50 wt.% PtRu/C with a 50 wt.% Nafion solution. Next, the mixture was smeared onto the nickel foam and dried at 80 °C for 2 h under vacuum. Finally, the anode was pressed under at 3 MPa. The mass loading of the PtRu/C in the anode was 6 mg cm⁻².

The anode, membrane and cathode were pressed together during cell assembly. The cathode faced 5 ml min⁻¹ of O₂. The anode was simultaneously supplied with an aqueous fuel solution containing 5 M methanol and 4 M KOH at 20 ml min⁻¹. Fig. 1 is the schematic of DMFC structure.

2.3. Electrochemical performance measurements

The cyclic voltammetry (CV) and linear sweep voltammetry (LSV) experiments were performed using a rotating ring-disk electrode (RRDE, Pine Research Instrumentation) connected to an electrochemical work station (CHI 750D, CH Instruments) with an AFMSRCE rotator (Pine Research Instrumentation). A Hg/HgO (1 M KOH) electrode and a Pt-mesh (1 × 1 cm²) were used as the reference and counter electrodes, respectively. The glassy carbon electrode was modified as follows. First, a catalyst ink was prepared by ultrasonically mixing 3 mg of catalyst, 0.1 mL of deionized water, 0.5 mL of isopropanol and 50 μL of Nafion (5 wt.%); 5 μL of this mixture was spread onto the surface of the glassy carbon electrode and allowed to dry overnight. The electrolyte solution (1 M KOH solution with or without methanol) was saturated with bubbling N₂ or O₂ for 30 min, respectively, prior to each CV and LSV experiment. The capacitive-corrected ORR currents were obtained by subtracting the current measured under N₂ from that found in pure O₂ under same condition. The scan rates were 50 mV s⁻¹ and 10 mV s⁻¹ for CV and LSV, respectively.

3. Results and discussion

3.1. Structure and morphology characterization

The structural features of the three samples are confirmed using their XRD patterns, as shown in Fig. 2; the diffractions of these samples agree with the standard patterns for a pure tetragonal cryptomelane phase (JCPDS card file 29-1020). The KMO-80 sample

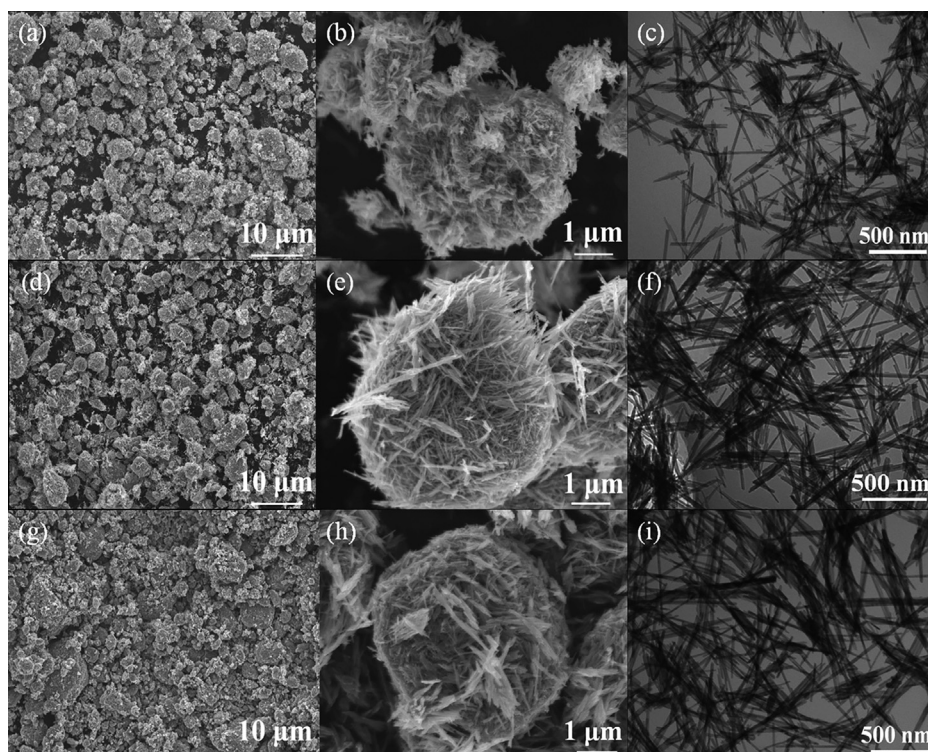


Fig. 4. FESEM images of (a and b) KMO-80, (d and e) KMO-100 and (g and h) KMO-120, respectively; TEM images of (c) KMO-80, (f) KMO-100 and (i) KMO-120, respectively.

exhibits weaker peaks than the KMO-100 sample. The XRD peaks sharpen and intensify when increasing the synthesis temperature to 100 °C, suggesting an enhancement in the crystallinity [34]. However, the peaks of KMO-120 are weaker and broader than that of KMO-100, this should attribute to the smaller grain size of KMO-120 [35]. Fig. 3 shows an EDXS analysis of the as-prepared KMO-100, revealing that the sample has a K:Mn:O composition of 3.9:31.44:64.66, similar to the atomic ratio of $\text{KMn}_8\text{O}_{16}$.

Fig. 4 shows the FESEM and TEM images of the KMO-80, KMO-100 and KMO-120. Compared to Fig. 4(a) and (d), the microspherical morphology of KMO-100 sample are more uniform than that of KMO-80. When temperature increases to 120 °C, aggregates of the microspheres form (Fig. 4(g)). The enlarged images in Fig. 4(b), (e) and (h) show individual ball structures 2–6 μm in diameter that consist of numerous long nanoscale rods. Fig. 4(h) shows that the nanorods in the microspheres formed in KMO-120 are very tightly wrapped compared to those in KMO-80 and KMO-100. The TEM images in Fig. 4(c), (f) and (i) show that the diameter and length of these nanorods ranged from 10 to 20 nm and approximately 300–1000 nm, respectively. The aspect ratio of these nanorods ranged from 15 to 100. The rods in KMO-120 are finer than those in the other two samples, which is in agreement with XRD measurement of Fig. 2 that the broader peaks of KMO-120 indicate smaller grain size.

3.2. Oxygen reduction reaction activity and methanol tolerance

Fig. 5(a) shows CV curves of KMO-80, KMO-100 and KMO-120 modified glassy carbon electrode in two solutions (0.5 M MeOH + 1 M KOH and 1 M KOH), respectively. An evident oxygen reduction peak potential at -0.35 V vs. Hg/HgO can be observed and KMO-100 exhibits a much higher oxygen reduction peak than other two samples. The results strongly indicate that the KMO-100 catalyst possesses excellent ORR activity in alkaline environment. Meanwhile, no apparent oxidation peak is generated when methanol is present, indicating that KMO-100 is inert toward methanol oxidation reaction and has excellent methanol tolerance property.

The LSV curves were also performed for the catalysts to determine its ORR activity. For comparison, the performance of commercial MnO_2 and Pt/C were also investigated. The lower part of Fig. 5(b) displays disk current (I_D) against applied potential and the upper part shows the ring current (I_R) as a function of applied potential during ORR in 1 M KOH solution at 1900 rpm on a RRDE. The ORR on all the catalysts are diffusion controlled when the potential is less than -0.4 V vs. Hg/HgO and are under mixed diffusion-kinetic control in the potential region from -0.1 V to -0.4 V vs. Hg/HgO. As shown in Fig. 5(b), the half-wave potential of KMO-100 are more positive than KMO-80 and KMO-120, indicating KMO-100 reveals more excellent ORR activity than KMO-80 and KMO-120, and is in good agreement with CV results. Moreover, the half-wave potential and diffusion limited current increase in order of $\text{MnO}_2 < \text{KMO-120} < \text{KMO-80} < \text{KMO-100} < \text{Pt/C}$, illustrating the increase of ORR activity.

O_2 can be reduced to OH^- through a four-electron process or to H_2O_2 through a two-electron process in an alkaline medium [36–38]. Since the ring current is proportional to the amount of the intermediate product H_2O_2 , additional RRDE data shown in Fig. 5(b) also illustrate the ORR pathway ($4e^-$ or $2e^-$) of these catalysts. In the present work, the H_2O_2 percentage ($X_{\text{H}_2\text{O}_2}$) and the electron transfer number (n) during the ORR are calculated as follows:

$$X_{\text{H}_2\text{O}_2} = 2I_R / (nI_D + I_R) \times 100\% \quad (1)$$

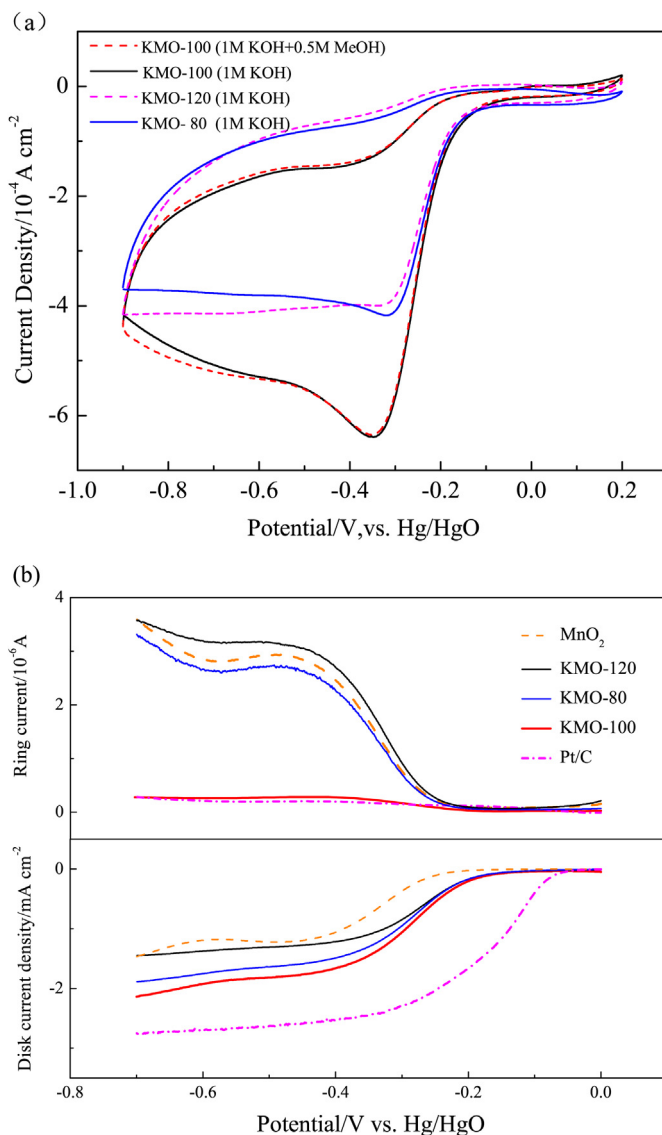


Fig. 5. (a) Cyclic voltammograms of KMO-80, KMO-100 and KMO-120 modified glassy carbon electrode in 1 M KOH and 1 M KOH + 0.5 M MeOH solutions saturated with O_2 at room temperature, respectively. Potential scan rate was 50 mV s^{-1} ; (b) Linear sweep voltammograms of KMO-80, KMO-100, KMO-120, MnO_2 and Pt/C modified glassy carbon electrode in 1 M KOH solutions saturated with O_2 at room temperature. Potential scan rate was 10 mV s^{-1} ; current densities were capacitive-corrected and normalizing to the surface area of the glassy carbon electrode. Counter electrode: Pt-mesh. Reference electrode: Hg/HgO electrode.

$$n = 4nI_D / (nI_D + I_R) \quad (2)$$

where I_D was the Faradaic current at the disk, I_R was the Faradaic current at the ring and $N = 0.26$ is the RRDE collection efficiency [39]. With regard to MnO_2 , KMO-120, KMO-80, KMO-100 and Pt/C at 0.5 V vs. Hg/HgO, the $X_{\text{H}_2\text{O}_2}$ are 8.71%, 8.5%, 7.9%, 0.66%, and 0.31%, and n values are 3.82, 3.83, 3.84, 3.98 and 3.99, respectively. KMO-100 shows the highest n (3.98) and the lowest $X_{\text{H}_2\text{O}_2}$ (0.66%) than KMO-80 and KMO-120, which is consistent with ORR activity results. Specially, the $X_{\text{H}_2\text{O}_2}$ and n values demonstrate that the electrochemical activity of KMO-100 for ORR exhibits a preference for a direct four-electron reduction pathway and is superior than MnO_2 and inferior than Pt/C.

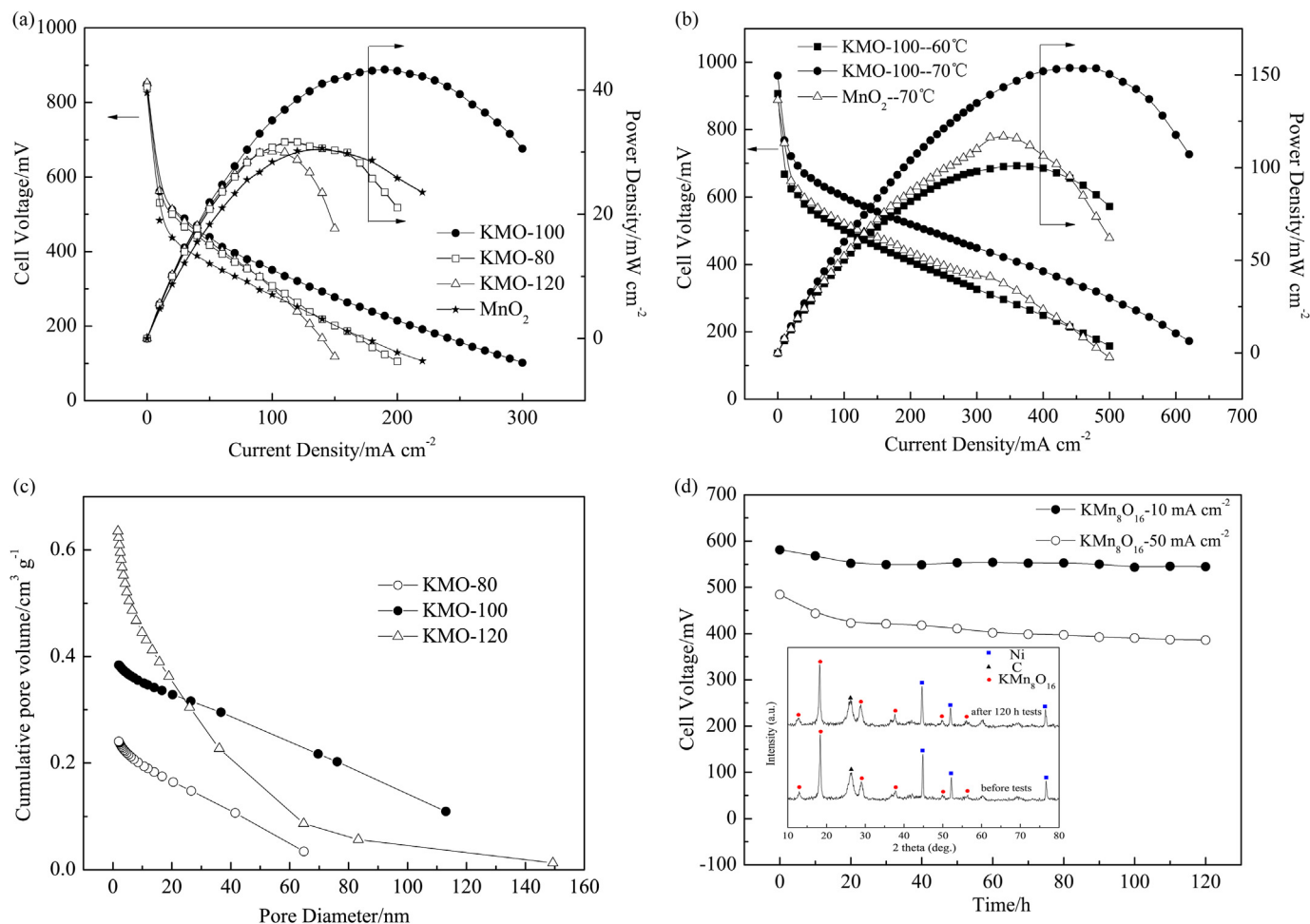


Fig. 6. (a) Comparison between the performances of DMFCs with KMO-80, KMO-100, KMO-120 and MnO₂ cathodic catalysts, respectively. Operating temperature: 25 °C; (b) Performances of DMFCs with KMO-100 and MnO₂ cathodic catalysts, respectively. Operating temperatures: 60 °C and 70 °C; (c) Cumulative pore volume – pore diameter plot of KMO-80, KMO-100 and KMO-120; (d) Stability tests for various current densities and XRD patterns of cathode before and after tests in DMFCs. The nickel XRD pattern corresponded to the nickel foam current collector. PtRu/C was used as anodic catalyst. The oxygen and fuel flow rates were 5 ml min⁻¹ and 20 ml min⁻¹, respectively.

3.3. Catalyst effect of KMn₈O₁₆ as cathode in DMFCs

The cell performance of the as-prepared samples used as cathodic catalysts in DMFCs was investigated. Fig. 6(a) shows the polarization and power density curves of KMO-80, KMO-100, KMO-120 and MnO₂ at room temperature. The KMO-120 and KMO-80 cathodes deliver peak power densities of 30.1 and 31.6 mW cm⁻². However, a peak power density of 43.3 mW cm⁻² is achieved at 190 mV vs. Hg/HgO with KMO-100. The peak power density is 30.6 mW cm⁻² when MnO₂ was used under the same condition.

The KMO-100 sample shows the best performance probably due to its larger surface area and proper pore size. The surface areas and pore diameters of the three samples were measured using a nitrogen physisorption technique. The surface areas measured with the BET method are 51.2, 60.7 and 206.5 m² g⁻¹ for KMO-80, KMO-100 and KMO-120. The KMO-80 has the smallest surface area, decreasing the contact area between the catalyst, electrolyte and O₂. A cumulative pore volume distribution is presented in Fig. 6(c). When the pore diameter is above 25 nm, the cumulative pore volume of KMO-100 is bigger than that of KMO-120, suggesting KMO-100 has more large pore. When the pore diameter is below 25 nm, KMO-120 has greater pore volume than that of KMO-100, illustrating the pore size distribution of KMO-120 is concentrated at 0–25 nm. The average pore sizes calculated from the adsorption

branch are 14.3, 26.9 and 9.3 nm for KMO-80, KMO-100 and KMO-120, respectively. Although KMO-120 has much higher surface area than KMO-80 and KMO-100, it performed more poorly due to its smaller pore diameter. The smaller pore diameter is unfavorable for O₂ and electrolyte flow, delaying the molecule or ionic motion, slowing electric charge exchange and decreasing the cell performance accordingly. Fig. 4(h) and (i) confirms the pore size measurements, revealing the tightly wrapped balls assembled using the finest rods. Therefore, the larger surface area is important, but the proper pore size of porous catalyst is also critical for ORR activity, which could increase the molecule or ionic motion rate.

Fig. 6(b) illustrates the performance of the cells using KMO-100 (assigned as KMn₈O₁₆) as a cathodic catalyst at higher temperatures. The peak power density is 101 mW cm⁻² when using KMn₈O₁₆ at 60 °C. Meanwhile, the peak power density is 153.9 mW cm⁻² at 70 °C. The MnO₂ catalyzed cathode delivers a peak power density of 116.7 mW cm⁻² at 70 °C. Importantly, these results are the highest achieved by non-noble metal cathodic catalysts and close to the highest reported values when both electrodes incorporate noble metal catalysts in acidic DMFCs [40–46].

Stability is another factor evaluating the cell performance. The stability was tested by monitoring voltage changes during galvanostatic discharge. Fig. 6(d) shows the results with KMn₈O₁₆ at constant current densities of 10 mA cm⁻² and 50 mA cm⁻² over

approximately 120 h at ambient temperature and atmosphere. As shown in Fig. 6(d), despite some slight degraded when increasing current density, no obvious attenuation is observed, suggesting that the cell is stable. XRD analysis is performed on the cathode before and after stability tests, as shown in the inset of Fig. 6(d). The result displays the crystal structure of $\text{KMnO}_4/\text{CNTs}$ does not change after the tests, indicating the cathodic catalyst is stable in methanol/alkaline solution.

4. Conclusion

1. Cryptomelane-type KMnO_4 microspheres assembled by nanorods are synthesized using a facile, template-free and single-step hydrothermal technique at 80, 100 and 120 °C. The diameters of the balls are 2–6 μm , and the nanorods are 10–20 nm in diameter and 300–1000 nm long.
2. The KMO-100 shows the highest n (3.98) and the lowest $X_{\text{H}_2\text{O}_2}$ (0.66%) than KMO-80 and KMO-120 during the ORR at 0.5 V vs. Hg/HgO , close to the desirable four-electron process during the application of O_2 to the cathode. The electrochemical experimental results demonstrate that KMO-100 not only shows good electrocatalytic activity and stability for oxygen reduction in alkaline solutions but also tolerates methanol poisoning well.
3. The peak power densities (43.3 mW cm^{-2} and 153.9 mW cm^{-2}) have been achieved at 25 °C and 70 °C, respectively, in DMFCs containing KMnO_4 microspheres synthesized at 100 °C as cathodic catalyst, PtRu/C alloy as anodic catalyst and PFM as membrane instead of conventional PEM. These results are the highest achieved by non-noble metal cathodic catalysts and are very close to the highest reported values when both electrodes incorporate noble metal catalysts in acidic DMFCs.

Acknowledgments

The authors are grateful for the financial support of the Key State Lab. Foundation of China.

References

- [1] X. Ren, P. Zelenay, S. Thomas, J. Davey, S. Gottesfeld, J. Power Sources 86 (2000) 111–116.
- [2] L. Li, Y. Xing, J. Phys. Chem. C 111 (2007) 2803–2808.
- [3] K.G. Nishanth, P. Sridhar, S. Pitchumani, A.K. Shukla, J. Electrochem. Soc. 158 (2011) B871–B876.
- [4] J.G. Liu, T.S. Zhao, R. Chen, C.W. Wong, Electrochem. Commun. 7 (2005) 288–294.
- [5] J. Ge, H. Liu, J. Power Sources 142 (2005) 56–69.
- [6] B. Gurau, R. Viswanathan, R. Liu, T.J. Lafrenz, K.L. Ley, E.S. Smotkin, E. Reddington, A. Sapienza, B.C. Chan, T.E. Mallouk, S. Sarangapani, J. Phys. Chem. B 102 (1998) 9997–10003.
- [7] C. Koenigsmann, S.S. Wong, Energy Environ. Sci. 4 (2011) 1161–1176.
- [8] Y. Fang, X. Yang, L. Wang, Y. Liu, Electrochim. Acta 90 (2013) 421–425.
- [9] X.D. Yang, Y.N. Liu, S. Li, X.Z. Wei, L. Wang, Y.Z. Chen, Sci. Rep. 2 (2012) 567.
- [10] H. Yang, N. Alonso-Vante, J.-M. Léger, C. Lamy, J. Phys. Chem. B 108 (2004) 1938–1947.
- [11] R. Dillon, S. Srinivasan, A.S. Arico, V. Antonucci, J. Power Sources 127 (2004) 112–126.
- [12] C.-C. Yang, J. Membr. Sci. 288 (2007) 51–60.
- [13] N. Jung, Y.-H. Cho, M. Ahn, J.W. Lim, Y.S. Kang, D.Y. Chung, J. Kim, Y.-H. Cho, Y.-E. Sung, Int. J. Hydrogen Energy 36 (2011) 15731–15738.
- [14] X. Li, Q. Huang, Z. Zou, B. Xia, H. Yang, Electrochim. Acta 53 (2008) 6662–6667.
- [15] M. Neergat, V. Gunasekar, R. Rahul, J. Electroanal. Chem. 658 (2011) 25–32.
- [16] K. Lee, L. Zhang, J. Zhang, J. Power Sources 165 (2007) 108–113.
- [17] K.-T. Jeng, N.-Y. Hsu, C.-C. Chien, Int. J. Hydrogen Energy 36 (2011) 3997–4006.
- [18] K. Kwon, Y.J. Sa, J.Y. Cheon, S.H. Joo, Langmuir 28 (2011) 991–996.
- [19] Y. Wei, C. Shengzhou, L. Weiming, Int. J. Hydrogen Energy 37 (2012) 942–945.
- [20] B. Scrosati, Electrochim. Acta 45 (2000) 2461–2466.
- [21] M. Saitoh, S. Yoshida, H. Yamane, M. Sano, M. Fujita, K. Kifune, Y. Kubota, J. Power Sources 122 (2003) 162–168.
- [22] F. Jiao, J. Bao, A.H. Hill, P.G. Bruce, Angew. Chem. 120 (2008) 9857–9862.
- [23] H. Sato, T. Enoki, J.-I. Yamaura, N. Yamamoto, Phys. Rev. B 59 (1999) 12836–12841.
- [24] F. Cheng, Y. Su, J. Liang, Z. Tao, J. Chen, Chem. Mater. 22 (2009) 898–905.
- [25] C.-L.S. O'Young, A. Robert, TEXACO DEVELOPMENT CORP, US, 1996.
- [26] J.E. Post, Proc. Natl. Acad. Sci. U. S. A. 96 (1999) 3447–3454.
- [27] N.N. Opembe, C.K. King'ondo, A.E. Espinal, C.-H. Chen, E.K. Nyutu, V.M. Crisostomo, S.L. Suib, J. Phys. Chem. C 114 (2010) 14417–14426.
- [28] C. Zhang, C. Feng, P. Zhang, Z. Guo, Z. Chen, S. Li, H. Liu, RSC Adv. 2 (2012) 1643–1649.
- [29] H. Tian, J. He, X. Zhang, L. Zhou, D. Wang, Micropor. Mesopor. Mater. 138 (2011) 118–122.
- [30] H.M. Galindo, Y. Carvajal, E. Njagi, R.A. Ristau, S.L. Suib, Langmuir 26 (2010) 13677–13683.
- [31] H. Zheng, C. Feng, S.-J. Kim, S. Yin, H. Wu, S. Wang, S. Li, Electrochim. Acta 88 (2013) 225–230.
- [32] S. Sithambaram, L. Xu, C.-H. Chen, Y. Ding, R. Kumar, C. Calvert, S.L. Suib, Catal. Today 140 (2009) 162–168.
- [33] R. Ghosh, Y.-C. Son, V.D. Makwana, S.L. Suib, J. Catal. 224 (2004) 288–296.
- [34] H. Liu, Y. Wang, L. Li, K. Wang, E. Hosono, H. Zhou, J. Mater. Chem. 19 (2009) 7885–7891.
- [35] H. Borchert, E.V. Shevchenko, A. Robert, I. Mekis, A. Kornowski, G. Grübel, H. Weller, Langmuir 21 (2005) 1931–1936.
- [36] S.L. Gojković, S. Gupta, R.F. Savinell, Electrochim. Acta 45 (1999) 889–897.
- [37] E. Claude, T. Addou, J.M. Latour, P. Aldebert, J. Appl. Electrochem. 28 (1998) 57–64.
- [38] U.A. Paulus, T.J. Schmidt, H.A. Gasteiger, R.J. Behm, J. Electroanal. Chem. 495 (2001) 134–145.
- [39] Pine Research Instrumentation, Taking Care of Your E6 Series “Change Disk” RRDE, 2005, <http://www.pineinst.com/echem/files/LMECE6.pdf>.
- [40] C.-C. Yang, J. Appl. Electrochem. 42 (2012) 305–317.
- [41] C.-C. Yang, S.J. Lue, J.-Y. Shih, J. Power Sources 196 (2011) 4458–4467.
- [42] H. Hou, G. Sun, R. He, Z. Wu, B. Sun, J. Power Sources 182 (2008) 95–99.
- [43] J.-S. Yu, M.-S. Kim, J.H. Kim, Phys. Chem. Chem. Phys. 12 (2010) 15274–15281.
- [44] K.-W. Park, Y.-W. Lee, Y.-E. Sung, Appl. Catal. B Environ. 132–133 (2013) 237–244.
- [45] Y.-C. Park, D.-H. Peck, S.-K. Kim, S. Lim, D.-H. Jung, D.-Y. Lee, Int. J. Hydrogen Energy 36 (2011) 5655–5665.
- [46] K.-W. Park, J.-H. Choi, S.-A. Lee, C. Pak, H. Chang, Y.-E. Sung, J. Catal. 224 (2004) 236–242.